Journal of Computational Mathematics
Vol.32, No.1, 2014, 21–38.

http://www.global-sci.org/jcm
doi:10.4208/jcm.1309-m4378

NUMERICAL RECONSTRUCTION OF SMALL PERTURBATIONS IN THE ELECTROMAGNETIC COEFFICIENTS OF A DIELECTRIC MATERIAL*

Marion Darbas
LAMFA UMR CNRS 7352 - Université de Picardie Jules Verne, Amiens, France
Email: marion.darbas@u-picardie.fr
Stephanie Lohrengel
LMR EA 4535 - Université de Reims Champagne-Ardenne, Reims, France
Email: stephanie.lohrengel@univ-reims.fr

Abstract

The aim of this paper is to solve numerically the inverse problem of reconstructing small amplitude perturbations in the magnetic permeability of a dielectric material from partial or total dynamic boundary measurements. Our numerical algorithm is based on the resolution of the time-dependent Maxwell equations, an exact controllability method and Fourier inversion for localizing the perturbations. Two-dimensional numerical experiments illustrate the performance of the reconstruction method for different configurations even in the case of limited-view data.

Mathematics subject classification: (MSC2010) 35Q61, 78M10, 35R30, 65M32, 65M60.
Key words: Maxwell's equations, Inverse problems, Numerical reconstruction, Exact boundary controllability, Fourier inversion.

1. Introduction and Presentation of the Inverse Problem

Inverse problems arise naturally in various areas of science and engineering and have many applications, e. g. in medical imaging, nondestructive testing or underground prospection. The control of the welding integrity of materials for example, is of the utmost importance for aeronautics and nuclear power safety. Several analytical and numerical studies have been devoted to the detection of inhomogeneities in the conductivity, or more generally, in the electromagnetic parameters of a body (see for example [2, 3, 7, 9, 11, 16, 29]). The localization procedure combines an asymptotic formula for the perturbation of the electromagnetic field with an inversion algorithm. The underlying direct problem is in general stationary or harmonic in time. In the present paper we consider such an approach for the resolution of a *time-dependent* electromagnetic inverse problem.

We focus on the numerical reconstruction of small amplitude perturbations in the electromagnetic parameters of a dielectric material from dynamic measurements on a part of the boundary. These problems appear typically in nondestructive testing and quality control of nonmetallic structures, for instance in the construction sector. In this context, reconstruction methods that allow partial boundary data are very interesting because, in most experimental settings, one does not have access to measurements on the whole boundary.

We apply an approach derived in [1]. Partial dynamic boundary measurements of the electric field are the - synthetic or experimental - data of the inversion algorithm. An asymptotic formula

* Received April 4, 2013 / Revised version received July 15, 2013 / Accepted September 16, 2013 / Published online January 22, 2014 /

expresses the effect of the small perturbations on these measurements. This yields a constructive numerical method for the localization of electromagnetic defects in the material. Recently, this has been tested successfully in the context of the wave equation for retrieving small conductivity imperfections [10]. The aim of the present paper is to generalize the method to the second order Maxwell equations. We present the algorithm in the case of a two-dimensional test domain. This is a first prospective study to show the effectiveness of the identification procedure. Since the underlying theoretical results have been obtained in three dimensions of space, it should be possible to realize the inspection of three-dimensional objects in the same way, provided one has a robust 3D Maxwell solver.

Let Ω be a bounded domain in $\mathbb{R}^2$ with a sufficiently smooth boundary $\Gamma := \partial\Omega$. Let $\boldsymbol{n}$ denote the outward unit normal to Γ. Let Ω' be a smooth subdomain of Ω. We assume that Ω is filled with a material of constant electric permittivity $\varepsilon = 1$ and magnetic permeability

$$\mu_\alpha(\boldsymbol{x}) = 1 + \alpha p(\boldsymbol{x}),\ \boldsymbol{x} \in \Omega. \tag{1.1}$$

The function p quantifies the perturbations of the permeability with respect to the homogeneous background medium ($\varepsilon = 1$, $\mu = 1$) and is supposed to satisfy the following conditions

$$p \in \mathcal{C}^1(\overline{\Omega}),\ p \equiv 0 \text{ in } \Omega \setminus \overline{\Omega'}, \text{ and } |p(\boldsymbol{x})| \leq M,\ \forall \boldsymbol{x} \in \Omega'. \tag{1.2}$$

The parameter $\alpha > 0$ designates the common order of magnitude of the perturbations which are assumed to be small compared to the background. Consequently, we may assume that there is $\underline{\mu} > 0$ such that $\mu_\alpha(\boldsymbol{x}) \geq \underline{\mu}$ for all $\boldsymbol{x} \in \Omega$. The electric charge and current density in Ω are supposed to be zero, and the problem is driven by an impressed source acting on the boundary (or a part of it) and prescribed initial states at $t = 0$.

Let $T > 0$ be the given final time and let $\boldsymbol{E}(\boldsymbol{x}, t)$ denote the electric field at a point $\boldsymbol{x} \in \Omega$ at time $t \in [0, T]$. In the absence of perturbations, the field $\boldsymbol{E}$ is solution to the following second-order system, derived from Maxwell's equations,

$$\begin{cases} \partial_t^2 \boldsymbol{E} + \mathbf{curl}(\operatorname{curl} \boldsymbol{E}) = \boldsymbol{0}, & \text{in } \Omega \times (0,T), \\ \operatorname{div} \boldsymbol{E} = 0, & \text{in } \Omega \times (0,T), \\ \boldsymbol{E} \times \boldsymbol{n} = F, & \text{on } \Gamma \times (0,T), \\ \boldsymbol{E}(0) = \boldsymbol{E}_0,\ \ \partial_t \boldsymbol{E}(0) = \boldsymbol{E}_1, & \text{in } \Omega. \end{cases} \tag{1.3}$$

Here, $\{\boldsymbol{E}_0, \boldsymbol{E}_1\}$ and F are respectively the boundary and initial data for the electric field. Notice that in two dimensions, the vector **curl** operator is defined for a scalar function φ by $\mathbf{curl}\, \varphi = (\partial_2 \varphi, -\partial_1 \varphi)^T$, whereas the scalar curl operator acting on a vector field $\boldsymbol{v} = (\boldsymbol{v}_1, \boldsymbol{v}_2)$ is given by $\operatorname{curl} \boldsymbol{v} = \nabla \times \boldsymbol{v} = \partial_1 \boldsymbol{v}_2 - \partial_2 \boldsymbol{v}_1$.

Next, consider the electric field $\boldsymbol{E}_\alpha$ in the presence of the perturbations and subject to the same boundary and initial data. $\boldsymbol{E}_\alpha$ is solution to the perturbed problem

$$\begin{cases} \partial_t^2 \boldsymbol{E}_\alpha + \mathbf{curl}(\mu_\alpha^{-1} \operatorname{curl} \boldsymbol{E}_\alpha) = \boldsymbol{0}, & \text{in } \Omega \times (0,T), \\ \operatorname{div} \boldsymbol{E}_\alpha = 0, & \text{in } \Omega \times (0,T), \\ \boldsymbol{E}_\alpha \times \boldsymbol{n} = F, & \text{on } \Gamma \times (0,T), \\ \boldsymbol{E}_\alpha(0) = \boldsymbol{E}_0,\ \ \partial_t \boldsymbol{E}_\alpha(0) = \boldsymbol{E}_1, & \text{in } \Omega. \end{cases} \tag{1.4}$$

Let us introduce the following functional spaces which are naturally involved in the setting of Maxwell's equations (see, for example, [25]):

$$J = \left\{ \boldsymbol{f} \in \left(L^2(\Omega)\right)^2 \mid \operatorname{div} \boldsymbol{f} = 0 \text{ in } \Omega \right\},$$

DOI https://doi.org/10.4208/jcm.1309-m4378 | Generated on 2025-01-22 19:02:04

as well as the subspaces of J,

$$J^1 = \Big\{ \boldsymbol{f} \in J \text{curl}\, \boldsymbol{f} \in L^2(\Omega) \Big\}, \text{ and}$$
$$J^1_\tau = \Big\{ \boldsymbol{f} \in J \text{curl}\, \boldsymbol{f} \in L^2(\Omega),\ \boldsymbol{f} \times \boldsymbol{n} = 0 \text{ on } \Gamma \Big\}.$$

For vanishing boundary data, the results in [12] yield the existence of a unique solution $\boldsymbol{E} \in \mathcal{C}^0(0,T;J^1_\tau) \cap \mathcal{C}^1(0,T;J)$ of problem (1.3) provided the initial data $(\boldsymbol{E}_0, \boldsymbol{E}_1)$ belong to the space $J^1_\tau \times J$. These results can be extended to the case of non-zero boundary data F which allow the construction of a regular lifting. Notice further that the assumptions on the perturbation p guarantee that $0 < \underline{\mu} \leq \mu_\alpha \leq 1 + \alpha M$. Thus, μ_α^{-1} is bounded from below and regular. Consequently, the theory from [12] (which relies on the variational approach in [24]) applies, and the perturbed problem (1.4) is well posed under the same regularity and compatibility assumptions on F and $\{\boldsymbol{E}_0, \boldsymbol{E}_1\}$.

In the sequel, we aim to reconstruct the perturbation p from total or partial boundary measurements $\text{curl}\, \boldsymbol{E}$ and $\text{curl}\, \boldsymbol{E}_\alpha$ on $\Gamma_0 \times (0,T)$ where Γ_0 is a part of the boundary Γ including the case $\Gamma_0 = \Gamma$. We propose to solve the following inverse problem:

$$(\mathcal{P}) \qquad \begin{cases} \text{Given a time } T > 0, \text{ boundary data } F \text{ and initial data } \{\boldsymbol{E}_0, \boldsymbol{E}_1\}, \\ \text{reconstruct the function } p(\boldsymbol{x}) \text{ for } \boldsymbol{x} \in \Omega', \text{ defined by (1.1)-(1.2)}, \\ \text{from the boundary measurements } \text{curl}\, \boldsymbol{E} \text{ and } \text{curl}\, \boldsymbol{E}_\alpha \text{ on } \Gamma_0 \times (0,T), \end{cases}$$

where $\boldsymbol{E}$ and $\boldsymbol{E}_\alpha$ are the solutions to problems (1.3) and (1.4), respectively. To this end, we consider the reconstruction method developped in [1].

The remainder of the paper is organized as follows. In section 2 we address the reconstruction method from a theoretical point of view. In section 3, we present some elements about the numerical resolution of problems (1.3) and (1.4), as well as the sampling method used for the identification procedure by Fourier inversion. Then, in the fourth section, various numerical results are reported to discuss the advantages and limits of the method. Finally, we give some conclusions and perspectives in the last section.

2. The Reconstruction Method

In this section, we describe the identification procedure adapted from [1]. This leads to a constructive numerical algorithm able to recover the small perturbations in the magnetic permeability which are quantified by the function p.

2.1. The reconstruction theorem

For an arbitrary wave vector $\boldsymbol{\eta} = (\boldsymbol{\eta}_1, \boldsymbol{\eta}_2)^t \in \mathbb{R}^2$, consider the source terms

$$F(\boldsymbol{x},t) = \boldsymbol{\eta}^\perp \times \boldsymbol{n} e^{i\boldsymbol{\eta}\cdot\boldsymbol{x} - i|\boldsymbol{\eta}|t}, \boldsymbol{E}_0(\boldsymbol{x}) = \boldsymbol{\eta}^\perp e^{i\boldsymbol{\eta}\cdot\boldsymbol{x}}, \text{ and } \boldsymbol{E}_1(\boldsymbol{x}) = -i|\boldsymbol{\eta}|\boldsymbol{E}_0(\boldsymbol{x}), \tag{2.1}$$

where the vector $\boldsymbol{\eta}^\perp$ is the unit vector orthogonal to $\boldsymbol{\eta}$. Assume that the boundary measurements

$$\text{curl}\, \boldsymbol{E} \text{ and } \text{curl}\, \boldsymbol{E}_\alpha \text{ on } \Gamma_0 \times (0,T), \tag{2.2}$$

have been recorded from the data (2.1).

DOI https://doi.org/10.4208/jcm.1309-m4378 | Generated on 2025-01-22 19:02:04

Notice that the corresponding exact background solution $\boldsymbol{E}$, solution to the unperturbed problem (1.3) for the source terms (2.1), is the plane wave

$$\boldsymbol{E}(\boldsymbol{x},t)=\boldsymbol{\eta}^{\perp}e^{i\boldsymbol{\eta}\cdot\boldsymbol{x}-i|\boldsymbol{\eta}|t}. \tag{2.3}$$

The reconstruction method, based on the knowledge of the boundary measurements (2.2), requires the resolution of an exact boundary controllability problem. Therefore, we assume that the part of the boundary Γ_0 where the measurements have been recorded, and the final time T geometrically control Ω in the sense of [14]. This roughly means that every geometrical optics ray, starting at any point $\boldsymbol{x}\in\Omega$ at time $t=0$, hits Γ_0 before time T at a non-diffractive point. The controllability problem then consists in finding a scalar function $G_{\boldsymbol{\eta}}$ such that $\boldsymbol{U}_{\boldsymbol{\eta}}(T)=\partial_t\boldsymbol{U}_{\boldsymbol{\eta}}(T)=0$ in Ω, where $\boldsymbol{U}_{\boldsymbol{\eta}}$ is the solution of the problem

$$\begin{cases}\partial_t^2\boldsymbol{U}_{\boldsymbol{\eta}}+\mathbf{curl}\,\mathrm{curl}\,\boldsymbol{U}_{\boldsymbol{\eta}}=\mathbf{0}, & \text{in } \Omega\times(0,T),\\ \mathrm{div}\,\boldsymbol{U}_{\boldsymbol{\eta}}=0, & \text{in } \Omega\times(0,T),\\ \boldsymbol{U}_{\boldsymbol{\eta}}\times\boldsymbol{n}=G_{\boldsymbol{\eta}}, & \text{on } \Gamma_0\times(0,T),\\ \boldsymbol{U}_{\boldsymbol{\eta}}\times\boldsymbol{n}=0, & \text{on } \Gamma\setminus\Gamma_0\times(0,T),\\ \boldsymbol{U}_{\boldsymbol{\eta}}(0)=\beta(\boldsymbol{x})\boldsymbol{E}_0(\boldsymbol{x})+\nabla\psi(\boldsymbol{x}),\ \ \partial_t\boldsymbol{U}_{\boldsymbol{\eta}}(0)=\mathbf{0}, & \text{in } \Omega,\end{cases} \tag{2.4}$$

for $\{\boldsymbol{E}_0,\boldsymbol{E}_1\}$ given as in (2.1). Here, $\beta\in\mathcal{C}_0^\infty(\Omega)$ is a cut-off function such that $\beta\equiv1$ on the subdomain Ω' of Ω that contains the perturbations. The existence of the control $G_{\boldsymbol{\eta}}$ is proven in [18] using the Hilbert Uniqueness Method [23]. In [1], the cut-off function β is introduced to truncate the initial data. However, the initial field $\beta(\boldsymbol{x})\boldsymbol{E}_0(\boldsymbol{x})$ is no more divergence-free. We therefore propose to add a correction term deriving from a scalar potential $\psi\in H_0^1(\Omega)$ to obtain $\mathrm{div}\,\boldsymbol{U}_{\boldsymbol{\eta}}(0)=0$ in Ω and $\boldsymbol{U}_{\boldsymbol{\eta}}(0)\in J$. The following theorem holds.

Theorem 2.1. *[1] Let $\boldsymbol{\eta}\in\mathbb{R}^2$. Let $\boldsymbol{E}_\alpha\in\mathcal{C}^0(0,T;J^1)\cap\mathcal{C}^1(0,T;J)$ be the unique solution to* (1.4) *with data* (2.1). *Suppose that Γ_0 and T geometrically control Ω. Then we have*

$$\int_0^T\int_{\Gamma_0}e^{i|\eta|t}\partial_t(e^{-i|\eta|t}G_{\boldsymbol{\eta}})(curl\,\boldsymbol{E}_\alpha-curl\,\boldsymbol{E})d\sigma dt=-\alpha|\boldsymbol{\eta}|^2\int_{\Omega'}p(\boldsymbol{x})e^{2i\boldsymbol{\eta}\cdot\boldsymbol{x}}dx+\mathcal{O}(\alpha^2), \tag{2.5}$$

where $G_{\boldsymbol{\eta}}$ is the boundary control in (2.4), *and $\boldsymbol{E}$ is the background solution to problem* (1.3). *The term $\mathcal{O}(\alpha^2)$ is independent of p and depends only of the bound M.*

Proof. The reconstruction formula (2.5) has been proven in [1] in a three-dimensional setting without the correction term $\nabla\psi$. The adaptation to the two-dimensional case is straightforward. However, the question is whether the presence of the term $\nabla\psi$ in the initial data of the control problem (2.4) influences the results or not. To this end, we will give in detail the proof of the following identity which is fundamental in the proof of (2.5),

$$\int_0^T\int_{\Gamma_0}G_{\boldsymbol{\eta}}\,\mathrm{curl}\,\boldsymbol{V}_{\boldsymbol{\eta}}\,d\sigma\,dt=-|\boldsymbol{\eta}|^2\int_{\Omega'}p(\boldsymbol{x})e^{2i\boldsymbol{\eta}\cdot\boldsymbol{x}}\,d\boldsymbol{x}, \tag{2.6}$$

where $\boldsymbol{V}_{\boldsymbol{\eta}}$ is the unique variational solution of the following auxiliary problem,

$$\begin{cases}\partial_t^2\boldsymbol{V}_{\boldsymbol{\eta}}+\mathbf{curl}\,\mathrm{curl}\,\boldsymbol{V}_{\boldsymbol{\eta}}=\mathbf{0}, & \text{in } \Omega\times(0,T),\\ \mathrm{div}\,\boldsymbol{V}_{\boldsymbol{\eta}}=0, & \text{in } \Omega\times(0,T),\\ \boldsymbol{V}_{\boldsymbol{\eta}}\times\boldsymbol{n}=0, & \text{on } \Gamma\times(0,T),\\ \boldsymbol{V}_{\boldsymbol{\eta}}(0)=\mathbf{0},\partial_t\boldsymbol{V}_{\boldsymbol{\eta}}(0)=i\,\mathbf{curl}\left(p(\boldsymbol{x})|\boldsymbol{\eta}|e^{i\boldsymbol{\eta}\cdot\boldsymbol{x}}\right), & \text{in } \Omega.\end{cases} \tag{2.7}$$

DOI https://doi.org/10.4208/jcm.1309-m4378 | Generated on 2025-01-22 19:02:04

In order to prove (2.6) notice that Green's formula yields

$$\begin{aligned}&\int_0^T \int_{\Gamma_0} G_{\boldsymbol{\eta}}\, \operatorname{curl} \boldsymbol{V}_{\boldsymbol{\eta}}\, d\sigma\, dt\\ &= \int_0^T \int_\Omega \boldsymbol{U}_{\boldsymbol{\eta}} \cdot \mathbf{curl} \operatorname{curl} \boldsymbol{V}_{\boldsymbol{\eta}}\, d\boldsymbol{x}\, dt - \int_0^T \int_\Omega \mathbf{curl} \operatorname{curl} \boldsymbol{U}_{\boldsymbol{\eta}} \cdot \boldsymbol{V}_{\boldsymbol{\eta}}\, d\boldsymbol{x}\, dt,\end{aligned}$$

since $\boldsymbol{U}_{\boldsymbol{\eta}} \times \boldsymbol{n} = G_{\boldsymbol{\eta}}$ and $\boldsymbol{V}_{\boldsymbol{\eta}} \times \boldsymbol{n} = 0$ on $\Gamma \times (0,T)$. Now, replacing the operator $\mathbf{curl} \operatorname{curl}$ by $-\partial_t^2$ and integrating by parts with respect to t yields

$$\begin{aligned}&\int_0^T \int_\Omega \boldsymbol{U}_{\boldsymbol{\eta}} \cdot \mathbf{curl} \operatorname{curl} \boldsymbol{V}_{\boldsymbol{\eta}}\, d\boldsymbol{x}\, dt - \int_0^T \int_\Omega \mathbf{curl} \operatorname{curl} \boldsymbol{U}_{\boldsymbol{\eta}} \cdot \boldsymbol{V}_{\boldsymbol{\eta}}\, d\boldsymbol{x}\, dt\\ &= \int_\Omega \boldsymbol{U}_{\boldsymbol{\eta}}(\cdot,0) \cdot \partial_t \boldsymbol{V}_{\boldsymbol{\eta}}(\cdot,0)\, d\boldsymbol{x}\\ &= i \int_\Omega \left(\beta(\boldsymbol{x})\boldsymbol{\eta}^\perp e^{i\boldsymbol{\eta}\cdot\boldsymbol{x}} + \nabla\psi(\boldsymbol{x})\right) \cdot \mathbf{curl}\left(p(\boldsymbol{x})|\boldsymbol{\eta}| e^{i\boldsymbol{\eta}\cdot\boldsymbol{x}}\right)\, d\boldsymbol{x},\end{aligned}$$

according to the prescribed initial values for $\boldsymbol{V}_{\boldsymbol{\eta}}$ and $\boldsymbol{U}_{\boldsymbol{\eta}}$, and the zero final states of $\boldsymbol{U}_{\boldsymbol{\eta}}$. From the right hand side of the last expression, it is clear that identity (2.6) is independent from the scalar potential ψ since

$$\int_\Omega \nabla\psi \cdot \mathbf{curl}\left(p(\boldsymbol{x})|\boldsymbol{\eta}| e^{i\boldsymbol{\eta}\cdot\boldsymbol{x}}\right)\, d\boldsymbol{x} = 0,$$

for any $\psi \in H_0^1(\Omega)$. Taking into account that $\beta \equiv 1$ on Ω' and $\operatorname{supp}(p) \subset \Omega'$, we finally get

$$\begin{aligned}&i \int_\Omega \beta(\boldsymbol{x})\boldsymbol{\eta}^\perp e^{i\boldsymbol{\eta}\cdot\boldsymbol{x}} \cdot \mathbf{curl}\left(p(\boldsymbol{x})|\boldsymbol{\eta}| e^{i\boldsymbol{\eta}\cdot\boldsymbol{x}}\right)\, d\boldsymbol{x}\\ &= i|\boldsymbol{\eta}| \int_{\Omega'} \operatorname{curl}\left(\boldsymbol{\eta}^\perp e^{i\boldsymbol{\eta}\cdot\boldsymbol{x}}\right) p(\boldsymbol{x}) e^{i\boldsymbol{\eta}\cdot\boldsymbol{x}}\, d\boldsymbol{x} = -|\boldsymbol{\eta}|^2 \int_{\Omega'} p(\boldsymbol{x}) e^{2i\boldsymbol{\eta}\cdot\boldsymbol{x}}\, d\boldsymbol{x},\end{aligned}$$

which yields (2.6).

The remainder of the proof consists in the estimation of the difference between the background solution $\boldsymbol{E}$ and the solution of the perturbed problem $\boldsymbol{E}_\alpha$ in an appropriate norm. This can be achieved in the same way as in [1].

Now, for a given wave vector $\boldsymbol{\eta}$, define the quantity $M_\alpha(\boldsymbol{\eta})$ by

$$M_\alpha(\boldsymbol{\eta}) = -\frac{1}{\alpha|\boldsymbol{\eta}|^2} \int_0^T \int_{\Gamma_0} e^{i|\boldsymbol{\eta}|t} \partial_t (e^{-i|\boldsymbol{\eta}|t} G_{\boldsymbol{\eta}})(\operatorname{curl} \boldsymbol{E}_\alpha - \operatorname{curl} \boldsymbol{E})\, d\sigma\, dt, \quad \forall \boldsymbol{\eta} \neq \mathbf{0}. \tag{2.8}$$

From (2.5) we infer that

$$M_\alpha(\boldsymbol{\eta}) \overset{\mathcal{O}(\alpha)}{\approx} \int_{\mathbb{R}^2} p(\boldsymbol{x}) e^{2i\boldsymbol{\eta}\cdot\boldsymbol{x}}\, d\boldsymbol{x},$$

where we neglected the asymptotically small remainder $\mathcal{O}(\alpha)$. Then, it can be easily seen from substitution and scaling rules that

$$M_\alpha(\boldsymbol{\eta}) \approx \pi^2 \widehat{p(-\pi\cdot)}, \tag{2.9}$$

where

$$\widehat{u}(\boldsymbol{\eta}) = \int_{\mathbb{R}^2} u(\boldsymbol{z}) e^{-2i\pi\boldsymbol{\eta}\cdot\boldsymbol{z}}\, d\boldsymbol{z},$$

DOI https://doi.org/10.4208/jcm.1309-m4378 | Generated on 2025-01-22 19:02:04

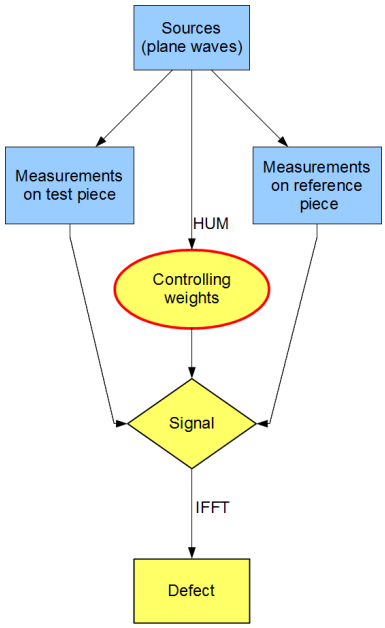

Fig. 2.1. Scheme of the reconstruction method.

denotes the Fourier transform of the function u defined in the physical domain. The reconstruction of the function p is then performed from inverse Fourier transformation,

$$p(-\pi \boldsymbol{x}) \approx \frac{1}{\pi^2} \check{M}_\alpha(\boldsymbol{x}), \tag{2.10}$$

where

$$\check{U}(\boldsymbol{x}) = \int_{\mathbb{R}^2} U(\boldsymbol{\eta}) e^{2i\pi \boldsymbol{\eta}\cdot\boldsymbol{x}}\, d\boldsymbol{\eta},$$

denotes the inverse Fourier transform of the function U defined in the frequency domain. The identification algorithm presented in the following sections is based on the relation (2.10) between the dynamic boundary measurements quantified by the function M_α and the perturbation p.

2.2. The identification procedure

For each $\boldsymbol{\eta}$ in a given discrete sampling domain $S \subset \mathbb{R}^2$ (see section 3.4), we form the quantity $M_\alpha(\boldsymbol{\eta})$ according to formula (2.8) by the following tasks

- Construct the boundary control $G_{\boldsymbol{\eta}}$ (cf. (2.4)) through H.U.M. (see section 3.2).
- Collect the boundary measurements $\operatorname{curl} \boldsymbol{E}$ on the surface of a healthy reference piece (experimental data), or alternatively, compute them by solving the Maxwell second-order system (1.3) with data (2.1) (synthetic data).
- Collect the boundary measurements $\operatorname{curl} \boldsymbol{E}_\alpha$ on the test piece, or compute them by solving the Maxwell second-order system (1.4) with the same data (see section 3.1).

Then, we are in possession of weighted boundary measurements $(M_\alpha(\boldsymbol{\eta}))_{\boldsymbol{\eta}\in S}$ that are the data of the inverse problem $(\mathcal{P})$. We compute the discrete inverse Fourier transform $(\check{M}_\alpha(\boldsymbol{x}))_{\boldsymbol{x}\in\Omega'}$ of $(M_\alpha(\boldsymbol{\eta}))_{\boldsymbol{\eta}\in S}$. The relation (2.10) ensures that the support of $\check{M}_\alpha$ yields the location of the perturbations defined by (3.5), after a rescaling by $-\pi$. Schematically, the reconstruction method can be represented as in Fig. 2.1. The weights $G_{\boldsymbol{\eta}}$ are computed by an iterative process which requires the resolution of two time-dependent Maxwell-type problems at each iteration. This heavy computation can be performed independently from the collection or numerical simulation of the boundary measurements. In particular, the weights are independent from the perturbation p and have to be computed only once for a given class of test pieces of same geometry and background permeability. This reduces the computational cost of the procedure.

3. Discretization Issues

In this section, we discuss discretization in space and time of the second order Maxwell equations (1.4) in a test piece with imperfections of type (1.2). We further recall basic ideas of the Hilbert Uniqueness Method for the construction of the control of the problem (2.4). Finally, we make precise the sampling for the inverse Fourier transformation.

3.1. Maxwell solver

Discretization in space of the second order Maxwell equations is performed by standard Lagrange finite elements of type Q1 on a structured mesh of rectangles. These elements are conforming in $(H^1(\Omega))^2$ which is not the natural space for the setting of Maxwell's equations. However, (1.4) is equivalent to a regularized formulation given on the vector space

$$\mathcal{H}(\mathrm{curl},\mathrm{div},\Omega)=\left\{\boldsymbol{v}\in\left(L^2(\Omega)\right)^2 \;\middle|\; \mathrm{curl}\,\boldsymbol{v}\in L^2(\Omega),\ \mathrm{div}\,\boldsymbol{v}\in L^2(\Omega)\right\}.$$

The regularized variational formulation reads as follows,

$$\left\{\begin{array}{l}\text{Find } \boldsymbol{E}_\alpha(\cdot,t)\in\mathcal{H}(\mathrm{curl},\mathrm{div},\Omega) \text{ such that } \boldsymbol{E}_\alpha\times\boldsymbol{n}=F \text{ on } \Gamma\times(0,T) \text{ and}\\ \dfrac{d^2}{dt^2}(\boldsymbol{E}_\alpha(\cdot,t),\boldsymbol{v})+(\mu_\alpha^{-1}\,\mathrm{curl}\,\boldsymbol{E}_\alpha,\mathrm{curl}\,\boldsymbol{v})+(\mathrm{div}\,\boldsymbol{E}_\alpha,\mathrm{div}\,\boldsymbol{v})=0,\ \ \forall\boldsymbol{v}\in\mathcal{H}_0(\mathrm{curl},\mathrm{div},\Omega)\\ \boldsymbol{E}_\alpha(\cdot,0)=\boldsymbol{E}_0,\ \ \partial_t\boldsymbol{E}_\alpha(\cdot,0)=\boldsymbol{E}_1 \text{ in } \Omega,\end{array}\right. \tag{3.1}$$

where

$$\mathcal{H}_0(\mathrm{curl},\mathrm{div},\Omega)=\left\{\boldsymbol{v}\in\mathcal{H}(\mathrm{curl},\mathrm{div},\Omega)\boldsymbol{v}\times\boldsymbol{n}=0 \text{ on } \Gamma\right\}.$$

The discretization in space of problem (3.1) by means of Lagrange finite elements is now possible since the domain Ω is assumed to be smooth ($\mathcal{C}^{1,1}$ or a convex polygon is sufficient) which insures the inclusion $\mathcal{H}_0(\mathrm{curl},\mathrm{div},\Omega)\subset(H^1(\Omega))^2$. Notice however that this inclusion fails to be true whenever the domain has reentrant corners (see [17]). The non-homogeneous boundary condition $\boldsymbol{E}_\alpha(\cdot,t)\times\boldsymbol{n}=F$ on Γ is taken into account *via* a lifting F_h such that $F_h(M_I,t)=F(M_I,t)$ if the node M_I belongs to Γ and $F_h(M_I,t)=0$ at the inner nodes of the mesh. For discretization in time, we use an implicit second order Newmark scheme.

We refer to [18] for a detailed discussion of the Maxwell solver.

DOI https://doi.org/10.4208/jcm.1309-m4378 | Generated on 2025-01-22 19:02:04

3.2. Discrete H.U.M.

The reconstruction method presented in Section 2 uses the boundary control of an exact controllability problem of the following type

$$\begin{cases} \text{Given } T>0 \text{ and initial data } \{\boldsymbol{E}_0, \boldsymbol{E}_1\}, \\ \text{find a control } G \text{ defined on } \Gamma_0 \times (0,T) \text{ such that} \\ \boldsymbol{U}(\cdot,T) = \partial_t \boldsymbol{U}(\cdot,T) = 0 \text{ in } \Omega, \end{cases} \tag{3.2}$$

where $\boldsymbol{U}$ is the solution to

$$\begin{cases} \partial_t^2 \boldsymbol{U} + \mathbf{curl}\,\mathrm{curl}\,\boldsymbol{U} = 0, & \text{in } \Omega\times(0,T), \\ \mathrm{div}\,\boldsymbol{U} = 0, & \text{in } \Omega\times(0,T), \\ \boldsymbol{U}\times\boldsymbol{n} = G\chi_{\Gamma_0}, & \text{on } \Gamma\times(0,T), \\ \boldsymbol{U}(\cdot,0) = \boldsymbol{E}_0, \quad \partial_t\boldsymbol{U}(\cdot,0) = \boldsymbol{E}_1, & \text{in } \Omega. \end{cases}$$

A constructive method for the effective computation of the control G is provided by the *Hilbert Uniqueness Method* (H.U.M.) of Lions [23], and we recall here the main steps of the algorithm. Full details on the numerical implementation as well as theoretical aspects can be found in [18].

The basic feature in H.U.M. is the construction of the linear H.U.M.-operator Λ which is defined as follows on an appropriate Hilbert space $B \subset J_\tau^1 \times J$:

1. For a given couple $\{\boldsymbol{\psi}_0, \boldsymbol{\psi}_1\}$, let $\boldsymbol{\psi}$ be the solution of the homogeneous adjoint problem

$$\begin{cases} \partial_t^2 \boldsymbol{\psi} + \mathbf{curl}\,\mathrm{curl}\,\boldsymbol{\psi} = 0, & \text{in } \Omega\times(0,T), \\ \mathrm{div}\,\boldsymbol{\psi} = 0, & \text{in } \Omega\times(0,T), \\ \boldsymbol{\psi}\times\boldsymbol{n} = 0, & \text{on } \Gamma\times(0,T), \\ \boldsymbol{\psi}(\cdot,0) = \boldsymbol{\psi}_0, \quad \partial_t\boldsymbol{\psi}(\cdot,0) = \boldsymbol{\psi}_1, & \text{in } \Omega. \end{cases} \tag{3.3}$$

2. Define the boundary data $G = -(\mathrm{curl}\,\boldsymbol{\psi})_{|\Gamma_0}$.

3. Solve the following backward problem with zero final data

$$\begin{cases} \partial_t^2 \boldsymbol{U} + \mathbf{curl}\,\mathrm{curl}\,\boldsymbol{U} = 0, & \text{in } \Omega\times(0,T), \\ \mathrm{div}\,\boldsymbol{U} = 0, & \text{in } \Omega\times(0,T), \\ \boldsymbol{U}\times\boldsymbol{n} = G\chi_{\Gamma_0}, & \text{on } \Gamma\times(0,T), \\ \boldsymbol{U}(\cdot,T) = \partial_t\boldsymbol{U}(\cdot,T) = \boldsymbol{0}, & \text{in } \Omega. \end{cases} \tag{3.4}$$

4. Set $\Lambda(\{\boldsymbol{\psi}_0, \boldsymbol{\psi}_1\}) = \{\partial_t\boldsymbol{U}(0), -\boldsymbol{U}(0)\}$.

Using fundamental results from [27], it is proven in [18] that the operator Λ is an isomorphism between B and its dual B'. In the simple case where Ω is a square, it is shown that B coincides with the classical space $J_\tau^1 \times J$.

The controllability result is the following

Theorem 3.1. [18] *Suppose that Γ_0 and T geometrically control Ω. Let $\{\boldsymbol{E}_0, \boldsymbol{E}_1\} \in J \times (J_\tau^1)'$. Then problem* (3.2) *has a solution $G \in L^2(0,T;L^2(\Gamma_0))$ which is obtained by setting $G = -(curl\,\boldsymbol{\psi})_{|\Gamma_0}$ where $\boldsymbol{\psi}$ is the solution to the homogeneous adjoint problem* (3.3)*. The couple $\{\boldsymbol{\psi}_0, \boldsymbol{\psi}_1\}$ that defines $\boldsymbol{\psi}$ is the inverse image of the initial data $\{\boldsymbol{E}_1, -\boldsymbol{E}_0\}$ through the H.U.M.-operator Λ, i.e.*

$$\Lambda(\{\boldsymbol{\psi}_0, \boldsymbol{\psi}_1\}) = \{\boldsymbol{E}_1, -\boldsymbol{E}_0\}.$$

Since the operator Λ defines a coercive bilinear form on B, $\Lambda^{-1}(\{\boldsymbol{E}_1, -\boldsymbol{E}_0\})$ is the solution of a variational problem that is resolved numerically by the conjugate gradient method. In order to overcome the difficulty of numerical instabilities related to spurious high-frequency oscillations, a bi-grid algorithm is used as preconditioner (see [19]). The discretization of the H.U.M.-operator Λ involves the numerical resolution of the adjoint problem on the one hand, and the backward problem on the other. This is performed by the Maxwell solver of Section 3.1.

3.3. The case of a piecewise constant perturbation

In the particular case where the magnetic permeability μ_α is a piecewise constant perturbation of the (known) background permeability $\mu = 1$, we are able to evaluate exactly the integral involved in formula (2.5). Indeed, let

$$\mu_\alpha(\boldsymbol{x}) = 1 + \alpha p(\boldsymbol{x}),\ \boldsymbol{x} \in \Omega,$$

with

$$p(\boldsymbol{x}) := \sum_{j=1}^{m} a_j \chi_{D_j}(\boldsymbol{x}). \tag{3.5}$$

Here, $D_j = [x_j - c_j h, x_j + c_j h] \times [y_j - d_j h, y_j + d_j h]$ denotes the support of the j-th imperfection of magnitude a_j and center $\boldsymbol{z}_j = (x_j, y_j)$, $1 \le j \le m$. The parameters c_j and d_j are real positive constants, and $h > 0$ is small compared to the dimensions of the test piece Ω. Moreover, the centers of the imperfections in the material's permeablity are assumed to satisfy two distance conditions: there is $d_0 > 0$ such that

$$\begin{cases} |\boldsymbol{z}_j - \boldsymbol{z}_\ell| \ge d_0 \ \ \forall\, j \ne \ell, \\ \operatorname{dist}(D_j, \Gamma) \ge d_0 \ \ \forall\, j. \end{cases} \tag{3.6}$$

Hence, the subdomain Ω' containing all the imperfections can be chosen such that $\operatorname{dist}(\partial\Omega', \Gamma) \ge d_0$.

For a given vector $\boldsymbol{\eta} = (\boldsymbol{\eta}_1, \boldsymbol{\eta}_2)^t$, a straightforward calculus yields

$$\int_{\Omega'} p(\boldsymbol{x}) e^{2i\boldsymbol{\eta}\cdot\boldsymbol{x}}\, d\boldsymbol{x} = \sum_{j=1}^{m} a_j \left(e^{2i\eta_1 x_j} \frac{\sin(2\eta_1 c_j h)}{\eta_1} \right) \left(e^{2i\eta_2 y_j} \frac{\sin(2\eta_2 d_j h)}{\eta_2} \right). \tag{3.7}$$

Taking into account that the Fourier transform of the indicator function is given by

$$\widehat{\chi}_{[-a/2,a/2]}(\xi) = \frac{\sin(\pi\xi a)}{\pi\xi},$$

and that $\widehat{\delta}_{-\frac{a}{\pi}}(\xi) = e^{2ia\xi}$ for the Delta distribution, we find from the right hand side in (3.7) that

$$\int_{\Omega'} p(\boldsymbol{x}) e^{2i\boldsymbol{\eta}\cdot\boldsymbol{x}} dx = \pi^2 \sum_{j=1}^{m} a_j \widehat{\delta}_{-\frac{x_j}{\pi}}(\eta_1) \widehat{\chi}_{[-\frac{c_j h}{\pi}, \frac{c_j h}{\pi}]}(\eta_1) \widehat{\delta}_{-\frac{y_j}{\pi}}(\eta_2) \widehat{\chi}_{[-\frac{d_j h}{\pi}, \frac{d_j h}{\pi}]}(\eta_2),$$

which yields the reconstruction of the perturbation $p(\boldsymbol{x})$ in this particular case.

Consequently, the quantity $M_\alpha(\boldsymbol{\eta})$ defined in (2.8) reads

$$M_\alpha(\boldsymbol{\eta}) = \sum_{j=1}^{m} a_j \left(e^{2i\eta_1 x_j} \frac{\sin(2\eta_1 c_j h)}{\eta_1} \right) \left(e^{2i\eta_2 y_j} \frac{\sin(2\eta_2 d_j h)}{\eta_2} \right) + \mathcal{O}(\alpha). \tag{3.8}$$

DOI https://doi.org/10.4208/jcm.1309-m4378 | Generated on 2025-01-22 19:02:04

3.4. Sampling

Let us recall that the perturbation p can be reconstructed from the quantity M_α due to the relation

$$p(-\pi \boldsymbol{x}) = \frac{1}{\pi^2} \check{M}_\alpha(\boldsymbol{x}), \tag{3.9}$$

where M_α is defined by formula (2.8). In order to compute numerically the inverse Fourier transform of M_α, we collect N_e^2 samples of $M_\alpha(\boldsymbol{\eta})$ for $\boldsymbol{\eta}$ belonging to the sampling domain $[-\eta_{\max}, \eta_{\max}[\times[-\eta_{\max}, \eta_{\max}[$.

According to the Nyquist-Shannon theorem, the perfect reconstruction of a real signal $x(t)$ from sampled values $(x(nT))_{n\in\mathbb{Z}}$ at a period T is possible whenever the sampling frequency $F_e = 1/T$ satisfies the relation

$$F_e \geq 2B. \tag{3.10}$$

Here, $(-B, B)$ is the bandwidth of the signal in the frequency domain. In our setting, the support of the function p is contained in a square of side length $2B$ with $B < 1$. Applying the Nyquist-Shannon theorem to the quantity $M_\alpha(\boldsymbol{\eta})$ sampled at the period $\Delta\eta = \frac{2\eta_{\max}}{N_e}$, we are able to reconstruct $\check{M}_\alpha(\boldsymbol{x})$ for $\boldsymbol{x} \in [-\frac{1}{2\Delta\eta}, \frac{1}{2\Delta\eta}] \times [-\frac{1}{2\Delta\eta}, \frac{1}{2\Delta\eta}]$. Taking into account the scaling factor $-\pi$ in (3.9) we recover the perturbation p in a square of length $\frac{\pi}{\Delta\eta}$. Consequently, choosing $\eta_{\max}$ and N_e in such a way that

$$\frac{\eta_{\max}}{N_e} \leq \frac{\pi}{4}, \quad \text{ensures} \quad \frac{\pi}{2\Delta\eta} \geq 1,$$

which is sufficient to reconstruct any perturbation in the test domain Ω. Concerning the resolution in space, we notice that $\Delta x = \frac{\pi}{2\eta_{\max}}$. The numerical results hereafter indicate that the critical distance d_0 of (3.6) is close to the resolution step Δx which can be expressed in terms of wavelength λ by $\Delta x = \frac{\lambda}{2\sqrt{2}}$ since $\lambda = \frac{2\pi}{|(\eta_{\max}, \eta_{\max})|}$. The reconstruction of closely spaced defects is thus limited by the sampling procedure. We refer to [8] for the analysis of a numerical method to solve the close-to-touching case.

Now, let $(M_{mn})_{m,n=1}^{N_e}$ be the samples of $M_\alpha(\boldsymbol{\eta})$ for $\boldsymbol{\eta} = (\eta_m, \eta_n)$ with $\eta_j = -\eta_{\max} + (j-1)\Delta\eta$, $j = 1, \ldots, N_e$. From inverse discrete Fourier transformation (IFFT), we get data (P_{kl}) with

$$P_{kl} = \sum_{m,n=1}^{N_e} M_{mn} \exp\left(\frac{2i\pi}{N_e}(k-1)(m-1)\right) \exp\left(\frac{2i\pi}{N_e}(l-1)(n-1)\right) \text{ for } k, l = 1, \ldots, N_e.$$

P_{kl} is an approximation of $\check{M}_\alpha$ at the point $(k\Delta x, l\Delta x)$. Swapping the data from the first and third (respectively the second and fourth) quadrant of the matrix $\frac{1}{\pi^2}P$ then yields the perturbation p at points $(-\pi k\Delta x, -\pi l\Delta x)$ with $k, l \in \{-N_e/2, \ldots, N_e/2 - 1\}$.

4. Numerical Reconstruction of the Defects

In this section we present the reconstruction of inhomogeneities for different configurations. The exact perturbation p is given by a piecewise constant function as in (3.5) which allows to compare the results with those obtained from the exact formula (3.8).

The numerical results have been obtained on the test domain $(-1, 1) \times (-1, 1)$ on a mesh of size $h_F = 1/32$. The parameter of the coarse mesh in the bi-grid algorithm is given by $h_G = 2h_F = 1/16$. The time step Δt is set to $1/64$ for a total time $T = 4$ for all the simulations.

DOI https://doi.org/10.4208/jcm.1309-m4378 | Generated on 2025-01-22 19:02:04

Recall that the reconstruction formula depends on the parameter α describing the common order of magnitude of the perturbations. Here, we tested the formula for $\alpha = 1/32$. The support of the different defects is a rectangle with sides of order h where $h = 1/32$ in all the numerical examples.

The sampling domain and sampling period have been adapted individually for the different test cases. A threshold η^* has been fixed for each test case, limiting the effective computation of $M_\alpha(\boldsymbol{\eta})$ for wave vectors $\boldsymbol{\eta}$ satisfying the condition

$$\|\boldsymbol{\eta}\| \leq \boldsymbol{\eta}^*.$$

This corresponds to the application of a radial window to the signal $(M_\alpha(\boldsymbol{\eta}))_{\boldsymbol{\eta}}$. The radial form of the window generalizes the standard one-dimensional rectangular window to two dimensions. In some cases, this choice causes undesirable effects near the border of the reconstruction domain. These effects can be diminished with a different window function, e. g. the Hamming window [20].

All the tests have been run on the ROMEO Computing Center[1)] .

4.1. Multiple defects

For the first configuration, we have two defects centered respectively at $\boldsymbol{z}_1 = (-0.5, -0.3)$ and $\boldsymbol{z}_2 = (0.5, 0.25)$. In Fig. 4.1, we compare the reconstruction from the exact formula (3.8) and its numerical approximation from (2.8). For both tests, we took a total number of 256 sample values (corresponding to $N_e = 16$ values in each direction) and a sampling domain with maximal frequency $\eta_{\max} = 6$. We have $\Delta\eta = 0.75$ which yields a reconstruction domain $[-B, B] \times [-B, B]$ with $B \approx 2$ and $\Delta x = 0.26$. The threshold parameter is $\eta^* = \|(5, 5)\|$.

Next, we tested a configuration with four defects which have been reconstructed from 256 sample values in a sampling domain given by $\eta_{\max} = 10$ (Fig. 4.2). This yields a reconstruction domain $[-B, B] \times [-B, B]$ with $B \approx 1.25$ and $\Delta x = 0.16$. The threshold parameter was set to $\eta^* = \|(8, 8)\|$.

The localization errors for both tests are reported in Table 4.1. Here and below, in the case of multiple defects, we report the error of the best (max) and the less well (min) located one. We see that the numerical algorithm performs very well for the reconstruction of multiple defects even in the case of a coarse sampling with only 16 values in each direction.

Table 4.1: Localization errors for multiple defects.

Example	Two defects	Four defects
Error $\boldsymbol{z}_j$ (max)	`4.49e-02`	`8.33e-02`
Error $\boldsymbol{z}_j$ (min)	`2.64e-02`	`3.21e-02`

4.2. Two close defects

Here, we aim to test the reconstruction algorithm in a limit configuration where the two imperfections centered at $\boldsymbol{z}_1 = (0.18, 0.23)$ and $\boldsymbol{z}_2 = (0.31, 0.44)$ are close to each other. More

[1)] https:/romeo.univ-reims.fr/

DOI https://doi.org/10.4208/jcm.1309-m4378 | Generated on 2025-01-22 19:02:04

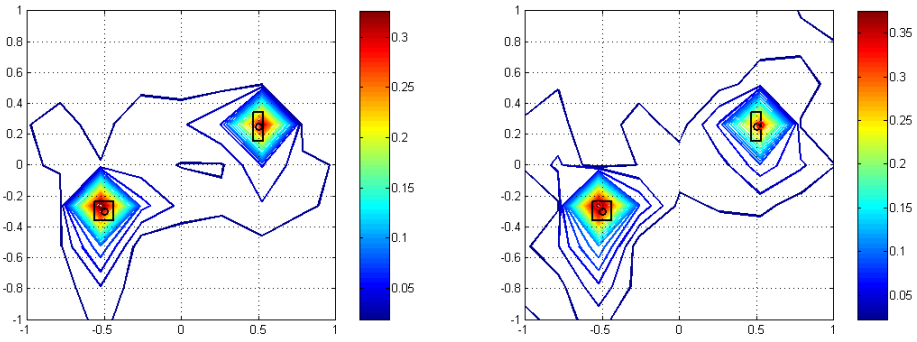

Fig. 4.1. Reconstruction of two defects (black rectangles) by IFFT: exact formula (left) and numerical approximation (right).

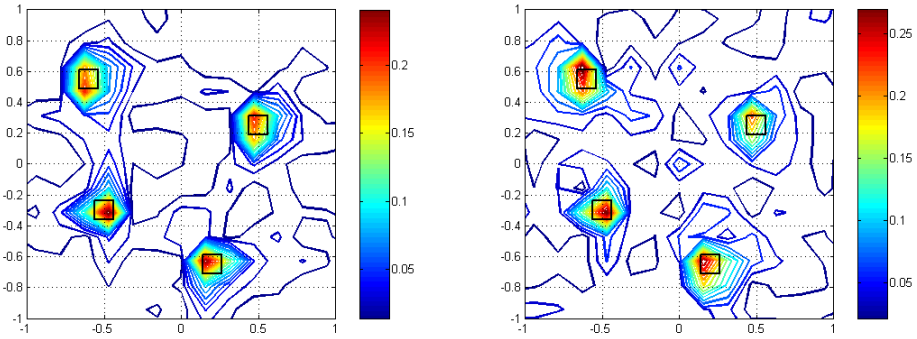

Fig. 4.2. Reconstruction of four defects (black rectangles) by IFFT: exact formula (left) and numerical approximation (right).

precisely, the supports of the imperfections given by

$$\begin{cases} D_1 = [0.12, 0.24] \times [0.17, 0.29], \ a_1 = 1.0, \\ D_2 = [0.25, 0.37] \times [0.35, 0.53], \ a_2 = 1.2, \end{cases}$$

yield a distance $d_0 = 0.06$ between the two defects.

We compare the numerical approximation for different sampling parameters. In the first configuration (Fig. 4.3, left), we took 256 ($N_e = 16$) sample values in a sampling domain with maximal frequency $\eta_{\max} = 8$ and truncation parameter $\eta^* = \|(6, 6)\|$. This corresponds to a sampling period of $\Delta\eta = 1$ and a reconstruction domain with $B \approx 1.5$ and $\Delta x = 0.2$. We clearly see that the numerical approximation only recovers a single perturbation located in between the two exact defects. For the second configuration (Fig. 4.3, right) we took 1024 sample values ($N_e = 32$) in a sampling domain given by $\eta_{\max} = 18$. The truncation parameter was set to $\eta^* = \|(12, 12)\|$. Consequently, the reconstruction domain is defined by $B = 1.39$ and $\Delta x = 0.09$. Now, the centers of both imperfections are well reconstructed and neatly separated by the numerical algorithm. The localization errors are reported in Table 4.2.

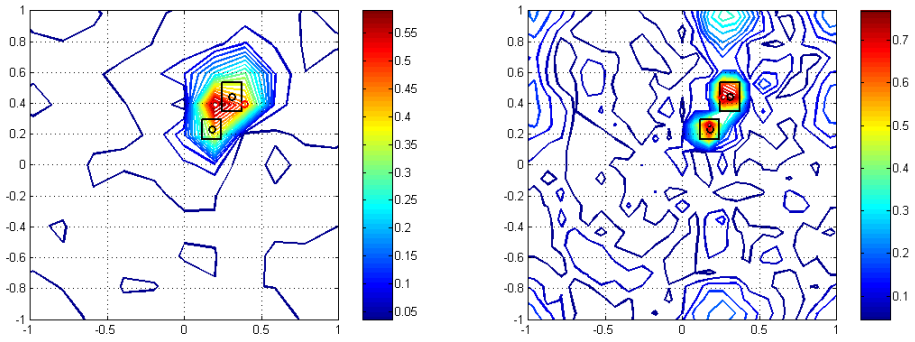

Fig. 4.3. Reconstruction of two close defects (black rectangles): coarse (left) and fine (right) sampling.

4.3. Defects close to the boundary

Another limiting configuration consists of defects which are close to the boundary. Here, we tested the reconstruction of four defects of identical intensity ($a_j = 1$):

$$\begin{cases} D_1 = [-0.56, -0.44] \times [-0.36, -0.24], & D_2 = [0.44, 0.56] \times [0.19, 0.31], \\ D_3 = [-0.86, -0.74] \times [0.34, 0.46], & D_4 = [0.14, 0.26] \times [-0.81, -0.69]. \end{cases}$$

Contrary to the test in section 4.1, two of them are close to the boundary: $\mathrm{dist}(D_3, \Gamma) = 0.14$ and $\mathrm{dist}(D_4, \Gamma) = 0.19$. A first sampling with $16^2 = 256$ sampling values, $\eta_{\max} = 6$ and $\eta^* = \|(5, 5)\|$ is able to reconstruct the perturbations D_1 and D_2 whereas D_3 and D_4 are not well localized. Indeed, in this case, the resolution is evaluated to $\Delta x = 0.26$, and only D_1 and D_2 satisfy $\mathrm{dist}(D_j, \Gamma) > \Delta x$. In Fig. 4.4 (right), we observe that a finer sampling with $32^2 = 1024$ sampling values, $\Delta x = 0.08$, $\eta_{\max} = 19$ and $\eta^* = \|(14, 14)\|$ yields a correct identification of all the defects. The localization errors are reported in Table 4.2.

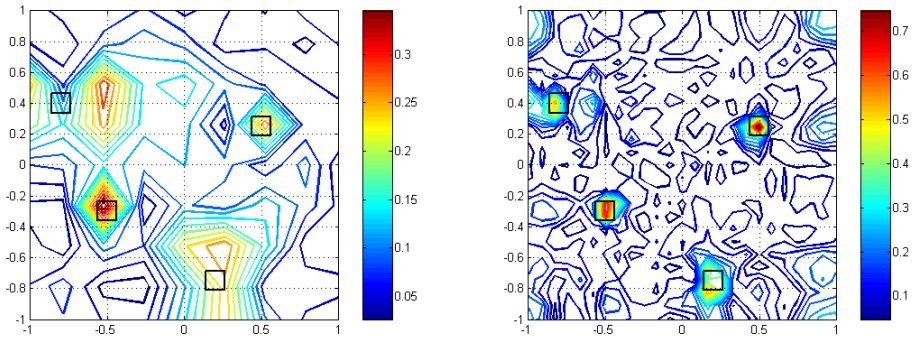

Fig. 4.4. Reconstruction of four defects (black rectangles) by IFFT: coarse (left) and fine (right) sampling. Two defects are close to the boundary.

DOI https://doi.org/10.4208/jcm.1309-m4378 | Generated on 2025-01-22 19:02:04

Table 4.2: Localization errors for limiting configurations.

Example	Two close defects		Defects close to boundary	
	coarse	fine	coarse	fine
Error $\boldsymbol{z}_j$ (max)	1.23e-01	4.80e-02	3.03e-01	8.42e-02
Error $\boldsymbol{z}_j$ (min)	–	3.22e-02	2.64e-02	4.43e-03

4.4. Reconstruction of the defect's shape and intensity

In order to test whether our algorithm is able to reconstruct the shape of a defect, we consider a configuration of two imperfections with different sizes (c_j, d_j). The first defect is extended in the x-direction whereas the second is quadratic. For a sampling configuration with 1024 sampling values, $\eta_{\max} = 18$ and threshold $\eta^* = \|(14, 14)\|$, we see from the results of Fig. 4.5 (right) that the numerical approximation recovers correctly the different shapes of the defects.

However, if the defects differ not only in their shapes but also in their intensities, the numerical algorithm does perform less well. To this end, we considered two defects with a ratio of $a_1/a_2 = 5$ between the intensity parameters a_1 and a_2. The position of the defects is the same as in the previous example (see Fig. 4.6 (right) for a schematic representation of the permeability function μ). We clearly see (Fig. 4.6, middle) that the numerical algorithm is able to reconstruct the shape and intensity of the predominant defect. The second "weak" perturbation, however, can be hardly detected and a spurious perturbation appears on the right of the predominant defect. These observations comply with the theoretical behavior of a rectangular window which is known to behave best for signals of comparable strength. A window function like the Hamming function improves the results (Fig. 4.6, right).

We further tested the reconstruction of a cross-like perturbation (Fig. 4.7, left) from a sampling with 1024 values, $\eta_{\max} = 19$ and threshold $\eta^* = \|(14, 14)\|$. Fig. 4.7 (middle) shows that the numerical reconstruction with the standard rectangular window is perfectly able to recover the shape of the cross. The spurious "reflections" at the boundary can be avoided by choosing a different window function (see Fig. 4.7 (right)). However, we may notice that in this case the characteristic shape of the cross is lost and only the position of the defect is

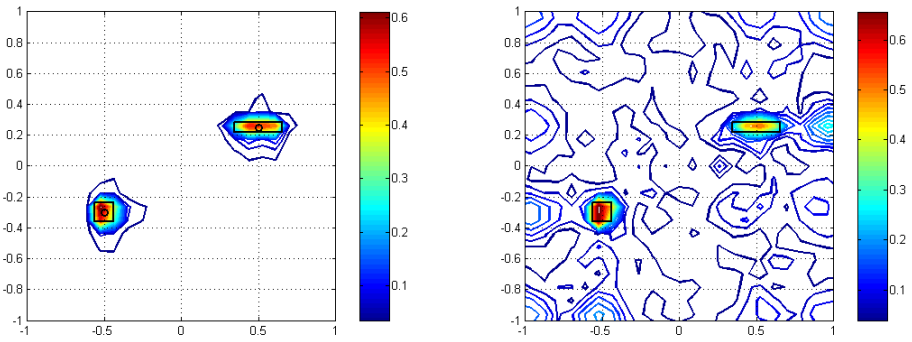

Fig. 4.5. Reconstruction of two defects of same intensity and different shapes (black rectangles): exact formula (left) and numerical approximation (right).

DOI https://doi.org/10.4208/jcm.1309-m4378 | Generated on 2025-01-22 19:02:04

Table 4.3: Localization errors for noisy data.

Example	0%	3%	5%
Error $\boldsymbol{z}_j$ (max)	4.49e-02	4.49e-02	5.7e-01
Error $\boldsymbol{z}_j$ (min)	2.64e-02	2.64e-02	4.5e-02

reconstructed.

4.5. Noisy data

An important feature in signal analysis is noise robustness. Noisy synthetic data have been generated by adding pointwise Gaussian errors to the exact data:

$$\operatorname{curl} \boldsymbol{E}(\boldsymbol{x}_k, t^n) - \operatorname{curl} \boldsymbol{E}_\alpha(\boldsymbol{x}_k, t^n) + \delta \max_k \max_n \left(|\operatorname{curl} \boldsymbol{E}(\boldsymbol{x}_k, t^n)| + |\operatorname{curl} \boldsymbol{E}_\alpha(\boldsymbol{x}_k, t^n)|\right) \xi_{kn}, \quad (4.1)$$

where $(\boldsymbol{x}_k)_k$ are the measurement points on Γ_0, t^n are the discrete time steps, ξ_{kn} are standard normal variables, and δ refers to the relative noise level. In Fig. 4.8 we compare the results for different values of δ on a sampling domain with 256 values, $\eta_{\max} = 6$ and threshold parameter $\eta^* = \|(5,5)\|$. One may notice that the reconstruction is robust up to 3% noise with the same localization error of order 10^{-2} as in the academic case with no noise (see Table 4.3). For 5% noise, the method still recovers rather well one of the two defects, whereas a spurious defect becomes predominant over the real second defect.

Table 4.4: Localization errors for partial measurements.

Example	total	partial (3 sides)	partial (north and south)
Error $\boldsymbol{z}_j$ (max)	9.04e-02	8.66e-02	8.66e-02
Error $\boldsymbol{z}_j$ (min)	4.29e-02	4.29e-02	4.29e-02

4.6. Partial measurements

Finally, let us consider partial boundary measurements for a configuration of three imperfections with identical intensity. We compare the results obtained from total control $\Gamma_0 = \Gamma$ with those obtained from partial control on three (resp. two) sides of the domain, $\Gamma_0 = \Gamma \setminus \{(1,y)\,|\,-1 \le y \le 1\}$ (resp. $\Gamma_0 = \{(x,-1)\,|\,-1 \le x \le 1\} \cup \{(x,1)\,|\,-1 \le x \le 1\}$). The sampling domain was given by 256 sampling values and $\eta_{\max} = 10$ with $\eta^* = \|(7,7)\|$. We notice that there is no significant difference between the results obtained with total (Fig. 4.9, left) and partial control on three sides (Fig. 4.9, middle), even if one of the perturbations is located near the boundary where no measurements are recorded. For partial boundary measurements on the north and south boundary, i. e. $\Gamma_0 = \{(x,-1)\,|\,-1 \le x \le 1\} \cup \{(x,1)\,|\,-1 \le x \le 1\}$, one of the three defects appears much weaker than the other two (Fig. 4.9, right), even if the localization error is nearly the same than for total control (see Table 4.4). It is worth noticing that this case does not enter in the framework of Theorem 2.1 since the final time T and Γ_0 do not control geometrically the domain Ω.

DOI https://doi.org/10.4208/jcm.1309-m4378 | Generated on 2025-01-22 19:02:04

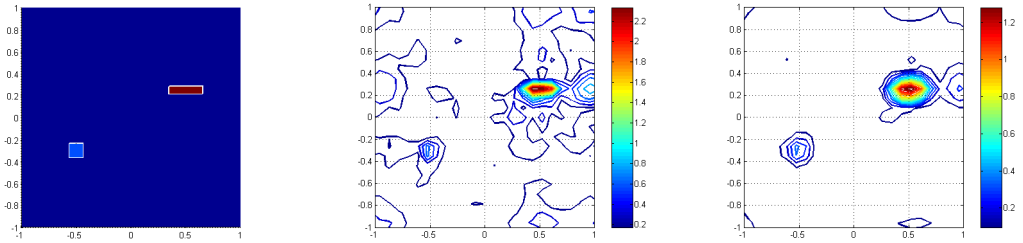

Fig. 4.6. Reconstruction of two defects of different shapes and intensities: exact shape (left), numerical approximation with radial window (middle) and the Hamming window function (right).

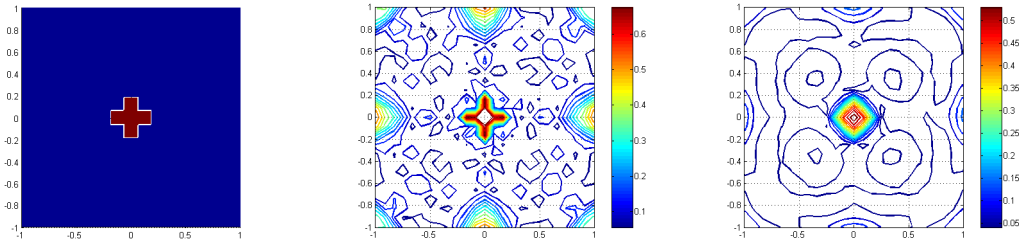

Fig. 4.7. Reconstruction of a cross-like defect: exact shape (left), numerical approximation with radial window (middle) and the Hamming window function (right).

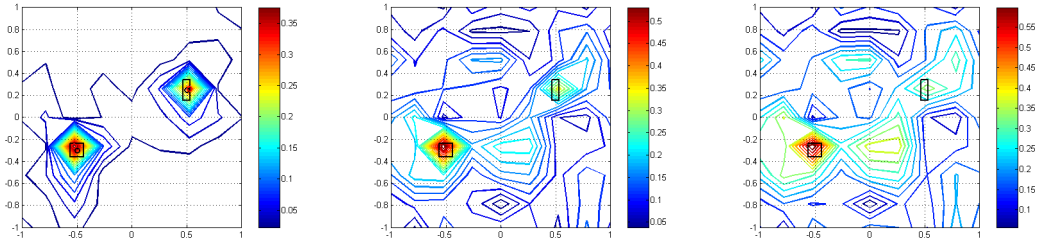

Fig. 4.8. Reconstruction of two imperfections (black rectangles) with different noise levels: 0% noise (left), 3% noise (middle), 5% noise (right).

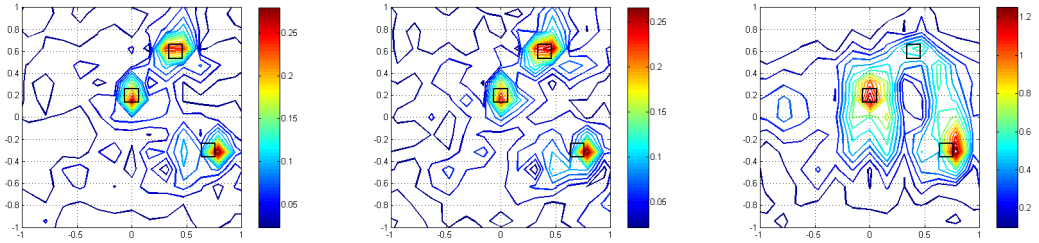

Fig. 4.9. Reconstruction of three imperfections (black rectangles) from total (left) and partial measurements on three sides (middle) and north and south boundary (right).

5. Conclusion and Perspectives

We have presented a dynamical reconstruction procedure based on theoretical results of Ammari [1]. This technique is able to localize small amplitude perturbations in the magnetic permeability of a dielectric material from total or partial boundary measurements. The key ingredient is the numerical construction of a boundary control for the second order Maxwell equations through H.U.M. The data of our inversion method are boundary measurements weighted by these control terms. An asymptotic formula ensures that the perturbations can be retrieved from discrete Fourier transformation of the data. This algorithm is numerically illustrated on several examples with multiple inclusions. The results yield accurate reconstructions in terms of the locations of the defects even in the case of coarse sampling, and give informations about their shapes. A finer sampling is required in some limit configurations (defects close to each other or to the boundary) to obtain a higher resolution in space. An attractive feature of the method is to allow the same accuracy from limited-view data than from full boundary data.

No specific application is realized to date but this numerical study represents a first step in the development of effective methods in non-destructive testing. The theoretical results leading to the asymptotic formula as well as the exact boundary controllability for Maxwell's equations have been proved for three-dimensional test pieces [1,18]. The reconstruction of three-dimensional defects should thus be obtained without additional difficulty, provided one has a robust 3D Maxwell solver. The extension to general non-cartesian geometries would allow to deal with real-life applications [26]. Another interesting point would be to analyze the stability of the localization procedure with respect to measurement noises. Promising recent results have been derived in [4–6] using the MUSIC algorithm. Finally, the convergence of the method is related to a complex interaction between H.U.M., IFFT and sampling. A careful numerical analysis of the reconstruction technique as in [21], for example, would provide further insights into its performance.

Acknowledgments. The authors would like to thank the anonymous referee for useful comments and suggestions. This work was supported by the research project "PINCEL", co-financed by the Picardie Region (France) and European Regional Development Fund.

References

[1] H. Ammari, Identification of small amplitude perturbations in the electromagnetic parameters from partial dynamic boundary measurements, *J. Math. Anal. Appl.*, **282** (2003), 479-494.

[2] H. Ammari, M. Asch, V. Jugnon, L. Guadarrama Bustos, and H. Kang, Transient imaging with limited-view data, *SIAM J. Imaging Sciences*, **4** (2011), 1097-1121.

[3] H. Ammari, E. Iakovleva, D. Lesselier and G. Perrusson, MUSIC-type electromagnetic imaging of a collection of small three-dimensional inclusions, *SIAM Journal on Scientific Computing,* **29** (2007), 674-709.

[4] H. Ammari, J. Garnier, H. Kang, W.K. Park, and K. Solna, Imaging schemes for perfectly conducting cracks, *SIAM J. Appl. Math.* **71**(1) (2011), 68-91.

[5] H. Ammari, J. Garnier, V. Jugnon, and H. Kang, Stability and resolution analysis for a topological derivative based imaging functional, *SIAM J. Control Optim.* **50**(1) (2012), 48-76.

[6] H. Ammari, J. Garnier, and K. Solna, A statistical approach to target detection and localization in the presence of noise, *Waves Random Complex Media* **22**(1) (2012), 40-65.

[7] H. Ammari and H. Kang, Reconstruction of Small Inhomogeneities from Boundary Measurements, Lecture Notes in Mathematics, Volume 1846, Springer-Verlag, Berlin 2004.

[8] H. Ammari, H. Kang, E. Kim, and M. Lim, Reconstruction of closely spaced small inclusions, *SIAM J. Numer. Anal.* **42**(6) (2005), 2408-2428.

[9] H. Ammari, M.S. Vogelius, and D. Volkov, Asymptotic formulas for perturbations in the electromagnetic fields due to the presence of inhomogeneities of small diameter. II. The full Maxwell equations, *J. Math. Pures Appl.* **80**(8) (2001), 769-814.

[10] M. Asch, M. Darbas and J.-B. Duval, Numerical resolution of an inverse boundary value problem for the wave equation in the presence of imperfections of small volume, *ESAIM: COCV* **17** (2011), 1016-1034.

[11] M. Asch and S. Mefire, Numerical localizations of 3D imperfections from an asymptotic formula for perturbations in the electric fields, *Journal of Computational Mathematics* **26** No.2 (2008), 149-195.

[12] F. Assous and P. Ciarlet, Jr., Quelques résultats sur la régularité en temps des équations de Maxwell instationnaires, *C.R. Acad. Sci. Paris*, **327** (1998), S´rie I, 719-724.

[13] F. Assous, P. Ciarlet Jr., E. Garcia, and J. Segré, Time-dependent Maxwell's equations with charges in singular geometries, *Comput. Methods Appl. Mech. Engrg.* 196 (2006), 665-681.

[14] C. Bardos, G. Lebeau and J. Rauch, Sharp sufficient conditions for the observation, control and stabilization of waves from the boundary, *SIAM J. Control Optim.*, **30** (1992), 1024-1065.

[15] A.P. Calderon, On an inverse boundary value problem, *Seminar on Numerical Analysis and its Applications to Continuum Physics*, Soc. Brasileira de Matemática, Rio de Janeiro, (1980), 65-73.

[16] D.J. Cedio-Fengya, S. Moskow and M.S. Vogelius, Identification of conductivity imperfections of small diameter by boundary measurements. Continuous dependence and computational reconstruction, *Inverse Problems* **14** (1998), 553-595.

[17] M. Costabel, A coercive bilinear form for Maxwell's equations, *J. Math. Anal. Appl.*, 157 (1991), 527-541.

[18] M. Darbas, O. Goubet and S. Lohrengel, Exact Boundary Controllability of the second-order Maxwell system: Theory and numerical simulation, *Comput. Math. Appl.* **63** (2012), no. 7, 1212-1237.

[19] R. Glowinski, C.H. Li and J.-L. Lions, A Numerical approach to the exact controllability of the wave equation (I). Dirichlet controls: Description of the numerical methods, *Japan J. Appl. Math.*, **7** (1990), 1-76.

[20] F. Harris, On the Use of Windows for Harmonic Analysis with the Discrete Fourier Transform, *Proceedings of the IEEE*, **66** (1978), 51-83.

[21] L.I. Ignat and E. Zuazua, Convergence of a two-grid method algorithm for the control of the wave equation, *J. Eur. Math. Soc.* **11** (2009), 351-391.

[22] R. Kohn and M. Vogelius, Determining conductivity by boundary measurements, *Comm. Pure Appl. Math.* **37** (1984), no.3, 289-298.

[23] J.-L. Lions, Contrôlabilité exacte, Perturbations et Stabilisation de Systèmes Distribués, Tome 1, Contrôlabilité exacte, Masson, Paris, 1988.

[24] J.-L. Lions and E. Magenes, Problèmes aux limites non homogènes et applications, Dunod, Paris, 1968.

[25] P. Monk, Finite Element Methods for Maxwell's Equations, Oxford University Press, New York, 2003.

[26] A. Nicolet and R. Belmans, Electric and Magnetic Fields : From Numerical Models to Industrial Applications, Plenum Publishing Corporation, New York, May 1995.

[27] K.D. Phung, Contrôle et stabilisation d'ondes électromagnétiques, *ESAIM: COCV*, 5 (2000), 87-137.

[28] J. Sylvester and G. Uhlmann, A global uniqueness theorem for an inverse boundary value problem, *Ann. Math.* **125** (1987), 153-189.

[29] D. Volkov, Numerical methods for locating small dielectric inhomogeneities, *Wave Motion* **38** (2003), 189-206.